Fast numerical simulations of 2D turbulence using a dynamic model for subfilter motions

J.-P. Laval [a,*], B. Dubrulle [b], S.V. Nazarenko [c]

[a] *Laboratoire de Mécanique de Lille, Blv Paul Langevin, F-59655 Villeneuve d'Ascq, France*
[b] *CEA/DRECAM/SPEC, L'Orme des Merisiers, 772, F-91191 Gif sur Yvette Cedex, France*
[c] *Mathematics Institute, University of Warwick, Coventry CV4 7AL, UK*

Abstract

We present numerical simulations of 2D turbulent flow using a new model for the subfilter scales which are computed using a dynamic equation linking the subfilter scales with the resolved velocity. This equation is not postulated, but derived from the constitutive equations under the assumption that the non-linear interactions of subfilter scales between themselves are small compared to their distortions by the resolved scales. Such an assumption results in a linear stochastic equation for the subfilter scales, which can be numerically solved by a decomposition of the subfilter scales into localized wave packets. The wave packets are randomly produced by the smallest of the resolved scales. They are further transported by the resolved-scale velocity and they have wavenumbers and amplitudes which evolve according to the resolved strain. Performance of our model is compared with direct numerical simulations of decaying and forced turbulence. For the same resolution, numerical simulations using our model allow for a significant reduction of the computational time (of the order of 100 in the case we consider), and allow to achieve of significantly larger Reynolds number than the direct method.
© 2003 Elsevier Inc. All rights reserved.

1. Introduction

The dynamics of high Reynolds number turbulent flow couples a large range of scales from the characteristic size of the domain to the dissipative scales. This range is usually too large to be fully resolved by direct numerical simulation (DNS) of the Navier–Stokes equations. This is the case for many applications in aeronautics, geophysics or astrophysics where the typical Reynolds numbers are of the order of 10^6–10^{12}. The largest Reynolds numbers which can be achieved by DNS are of the order of 10^4–10^5 [1,2]. The difficulty of direct simulation of turbulent flows at high Reynolds number arises because of two scaling laws: first, the memory requirement to be able to deal with all the scale of motions growths like $Re^{9/4}$, where Re is

---

the Reynolds number; second, the time stepping to be used to advance the equations has to be computed using the smallest resolved scale. As a result, computational time usually growths like Re^3. Despite of the growth of the computer power [3], the direct simulation of all realistic problems will not be conceivable before a long time.

Part of these difficulties could be circumvented if one could find an efficient approximate scheme to model the small scales of the turbulent flow, which usually monopolize 90% of the computations and, for most applications, do not need to be known with the same precision as the large scales. From an algorithmic point of view, several methods have been proposed to try to describe the small turbulent scales with less degree of freedom than in a DNS like for example, sparse Fourier transform [4], rarefied modes [5], wavelets [6], self-adaptive grid mesh [7,8]. From a theoretical point of view, the effort has been made to model action of the small scales onto the larger scales of motion (or onto the small scales themselves) to be able to deal with simpler and cheaper systems to compute. In the extreme case of large eddy simulations (LES) or Reynolds averaged Navier–Stokes (RANS) method, the effect of the small scales at large scales is directly modeled as a function of the resolved or mean scales of motions, resulting in both memory and computational gain. This is often done at the price of introduction of arbitrary parameters, which require calibration and which lower the predictive power of the simulation. Also, some models are not theoretically satisfying, since they break for example the basic symmetries of the original equations [9].

In this paper, we continue a study initiated in [10] and develop a new dynamic model for the turbulent subfilter quantities which is directly derived from the constitutive equations of motions. This model respects all the basic symmetries of the original equations, as well as their conservation properties. The main assumption underlying the model is that the smaller turbulent scales are much less energetic than the resolved scales, and so, that their main interactions are with the resolved flow. It then appears reasonable to try to model these main interactions with as few approximations as possible, while more freedom is allowed regarding their mutual interactions. In the model we consider, the interactions between the resolved and subfilter scales are taken into account without any approximation, while the mutual interactions between subfilter scales are replaced by a turbulent viscosity. In 2D geometry, where energy condensation at large scale guarantees that the dynamics of the small scales is mainly non-local in scales this turbulent viscosity is so small that it can be set to zero in some simple cases [11]. This allows a parameter free model of the subfilter scales, which will be described in the first part of this paper. In 3D situations where dynamic processes at small scales, like vortex stretching, are important to regulate any small-scale instability, or even in 2D when "large" and "small" scales are not well enough separated, the turbulent viscosity cannot be set to zero [12]. This option introduces a free parameter into the model, but, since it appears at a sub-dominant level, we may expect that its choice is not so critical for success of the model.

After parameterization of the non-linear interactions between the subfilter scales, their resulting equation of motion becomes linear. This essential feature has two advantages: first, it enables, in certain simple flow geometries, analytical solutions for the subfilter-scale dynamics as a function of the resolved quantities, thereby closing the equations of motions at the resolved-scale level. This property was used to obtain analytical solution for mean profiles in channel flows [13–15] or for the Planetary Surface Layer [16,17]. Second advantage of the linear description is that it allows for more efficient algorithms of integrations, using Lagrangian methods where the time stepping is done via a criterion based on the resolved scales. This allows numerical computations with a larger time step than DNS, and thus, at a lower computational cost. An essential part of our model is the averaged Reynolds stresses describing the feedback of the subgrid scales onto the resolved component. In [10], we considered the scale separation parameter to be much less than the non-linearity of the small scales and derived a feedback term in which the quadratic in the small-scale amplitude terms gave the main contribution into the Reynolds stress. Then, the model that consisted of two coupled "fluids" (the resolved and the subgrid one) was used to solve several problems with [18] and without scale separation [10], the later being the typical problems such as the forced turbulence, the vortex merger and a turbulence decay. It was noticed that in the problems without a natural scale separation, such

a model described very well the small-scale dynamics whereas improvements in modeling of the large scales (which is the main aim of the LES) was much more modest. The situation was clarified in [11] where direct numerical evaluations of the different contributions to the Reynolds stress were made. It was shown that in the problems without the scale separation the dominant contribution to the Reynolds stress comes from the linear rather than quadratic in the small-scale amplitude term. In the present contribution, we generalize the numerical approach introduced in [10] to the case of a continuous energy spectrum, and introduce a more efficient procedure to discretize the subfilter fields. Our goal here is to test our model both as a numerical method for an improved DNS, in the sense that we can compute the whole range of scales at a lower computational cost, and as a pseudo-LES method, in the sense that we compute only the larger scales, at an even lower computational cost. For the sake of simplicity, we shall consider here only the 2D case, where both the hypothesis of the turbulent model [11] and its consequences [18,10] have been studied in detail. The generalization to the 3D case is the subject of an ongoing research.

2. The turbulence model

2.1. Scale decomposition

We consider a 2D incompressible flow obeying the equations

$$
\begin{cases} \partial_t \omega + \mathrm{div}\,(\mathbf{u}\omega) = v\Delta\omega, \\ \mathrm{div}\,\mathbf{u} = 0, \end{cases}
\tag{1}
$$

where $\mathbf{u}$ is the velocity and v is the viscosity. In 2D geometry, the vorticity has only one non-zero component that we denote by ω. The resolved- and the subfilter-scale parts of the velocity and the vorticity fields are defined via a filtering procedure:

$$
\mathbf{U}(\mathbf{x},t) = \overline{\mathbf{u}(\mathbf{x},t)} = \int G(\mathbf{x}-\mathbf{x}')\mathbf{u}(\mathbf{x}',t)\,\mathrm{d}\mathbf{x}',
\tag{2}
$$

$$
\Omega(\mathbf{x},t) = \overline{\omega(\mathbf{x},t)} = \int G(\mathbf{x}-\mathbf{x}')\omega(\mathbf{x}',t)\,\mathrm{d}\mathbf{x}'.
\tag{3}
$$

Here, G is a filter, such that the resolved scales contain the main part of the total energy. In Section 3.4.1, we shall propose a special shape of G obeying this condition, and which is well adapted to our numerical method. Each field is then decomposed as follows:

$$
\mathbf{u}(\mathbf{x},t) = \mathbf{U}(\mathbf{x},t) + \mathbf{u}'(\mathbf{x},t),
\tag{4}
$$

$$
\omega(\mathbf{x},t) = \Omega(\mathbf{x},t) + \omega'(\mathbf{x},t),
\tag{5}
$$

where the primes denote subfilter-scale quantities. If we assume that the filter and the derivative commute, inserting this decomposition into the Navier–Stokes equations and separating the resolved- and the subfilter-scale parts (by subtracting the filtered Navier–Stokes equations to the original ones), we get a set of coupled equations

$$
\partial_t \Omega + \mathrm{div}\,(\overline{\mathbf{U}\Omega}) + \mathrm{div}\,(\overline{\mathbf{u}'\Omega}) + \mathrm{div}\,(\overline{\mathbf{U}\omega'}) + \mathrm{div}\,(\overline{\mathbf{u}'\omega'}) = v\Delta\Omega,
\tag{6}
$$

and

$$
\begin{aligned}
\partial_t \omega' &+ \mathrm{div}\,(\mathbf{U}\Omega) - \mathrm{div}\,(\overline{\mathbf{U}\Omega}) + \mathrm{div}\,(\mathbf{U}\omega') - \mathrm{div}\,(\overline{\mathbf{U}\omega'}) + \mathrm{div}\,(u'\Omega) \\
&- \mathrm{div}\,(\overline{u'\Omega}) + \mathrm{div}\,(u'\omega') - \mathrm{div}\,(\overline{u'\omega'}) = v\Delta\omega'.
\end{aligned}
\tag{7}
$$

The second up to the seventh terms of the l.h.s. of (7) are the contributions due to non-local interactions between the resolved and the subfilter scales. The last two terms in the l.h.s. of (7) are the contributions due to non-linear (local in scale space) interactions among the subfilter scales. In the favorable case where most of the energy is at the resolved scales, these last two terms can be expected to be negligible with respect to, e.g., the second up to the fifth terms of the l.h.s. of (7). Indeed, in a recent detailed numerical analysis of the system (6) and (7), Laval et al. [11] showed that for a very steep filter (when the filter G is a cut-off in the spectral space), the small-scale dynamics (and thus the large-scale dynamics) is independent of the local interactions between the small scales. When the later are neglected, the small-scale velocity and vorticity fields are not significantly changed, in both forced and decaying turbulence, even after several eddy turnover times [11]. The analysis has also shown that in 2D turbulence, the leading order contribution at large scales comes from the correlations involving the large-scale velocity field, i.e. $\mathbf{U}\Omega$ and $\mathbf{U}\omega'$. The next leading order contribution comes from the correlations between the small-scale velocity and vorticity $u'\omega'$, while the correlation between the small-scale velocity and large-scale vorticity $u'\Omega$ gives the lowest contribution. This ordering remains valid at small scales up to approximately half of the cut-off scale, where the $\mathbf{U}\Omega$ becomes zero (for geometrical reasons). The largest contribution then comes from the $\mathbf{U}\omega'$ term, followed by the terms involving $u'\omega'$ and $u'\Omega$.

2.2. A priori numerical estimates

In the present case, the filter G is smoother and subfilter scales include both large and small scales. It is thus important to conduct additional numerical evaluation of the various terms of (6) and (7) using a smooth filter, to check the validity of the non-locality assumption for the subfilter scales. We performed an a priori test with the filter used in our model. The choice of the filter will be discussed in Appendix D.

The test was done using a vorticity field from a decaying DNS on a 4096^2 grid at $R_\lambda \simeq 1.5 \times 10^5$ (see Fig. 1). Fig. 3 gives the distribution of each non-linear terms involved in the resolved-scales and the subfilter-scales equations (the result of the filtering process on the energy spectra is shown Fig. 2).
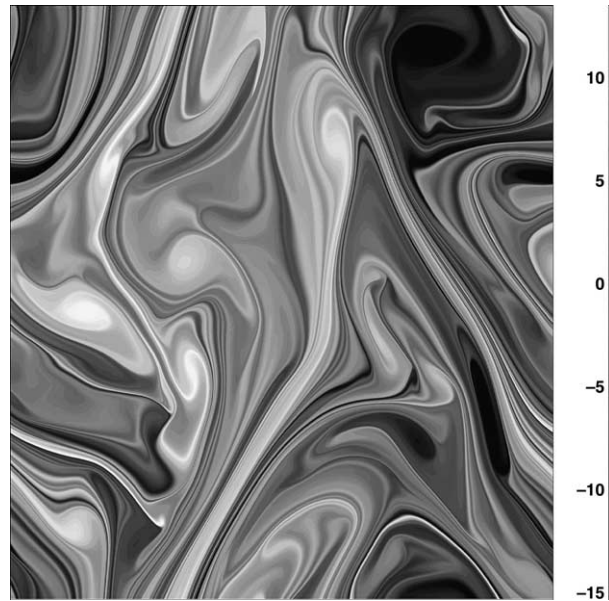

Fig. 1. Vorticity field of the DNS of decaying turbulence on a 4096^2 grid used for the a priori validation of Fig. 3.
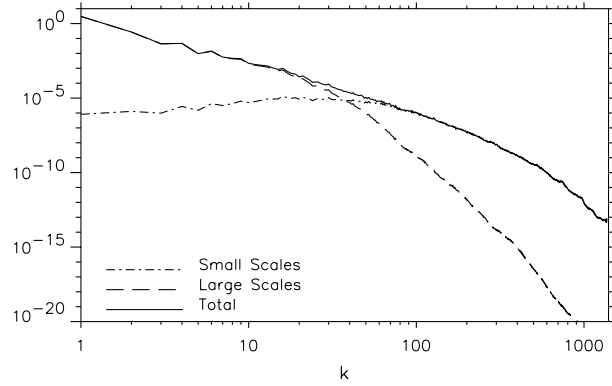
Fig. 2. Energy spectra of both resolved scales and subfilter scales for the DNS of decaying turbulence on a 4096^2 grid used for the a priori validation of Fig. 3. The filter used for the scale separation is defined in Eq. (22) with $dh = 2\pi/64$.
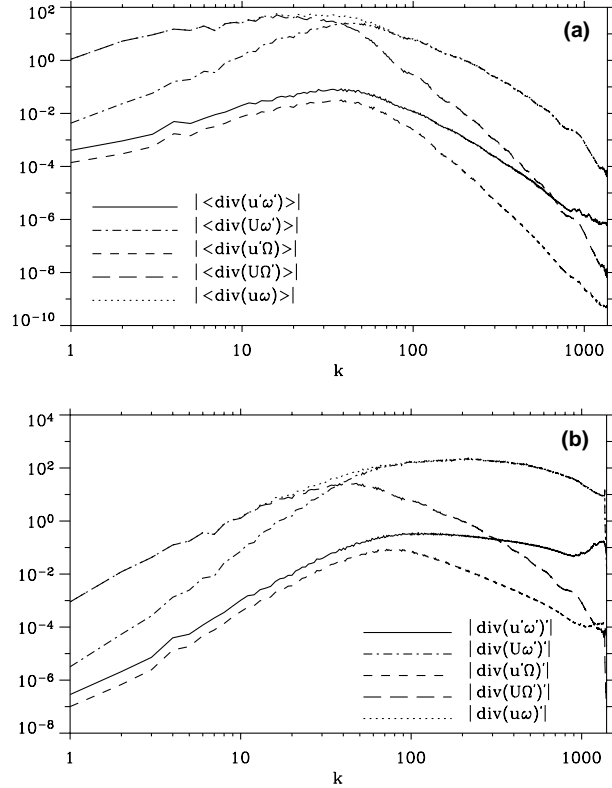

Fig. 3. Comparison of the intensity of the resolved scales (upper graph) and the subfilter scales (lower graph) of each component of the non-linear part of the decomposed equations (7) and (6). The filter used for the scale separation is a smooth filter in Fourier space defined by Eq. (22) and the results of the filtering are shown Fig. 2. ($|A'|$ and $|\langle A \rangle|$ means, respectively, the sum over a shell k of the modulus of the subfilter part and the resolved part of A).

Even with a smooth filter, the non-linear term involving only subfilter scales are still small compared to the leading order term $U\omega'$. The space repartition of relative intensity of $\mathrm{div}(\mathbf{u}'\omega')'$ compare to the whole non-linear term $\mathrm{div}(\mathbf{u}\omega)$ is shown Fig. 4. This ordering means that the dominant contribution to the dy-
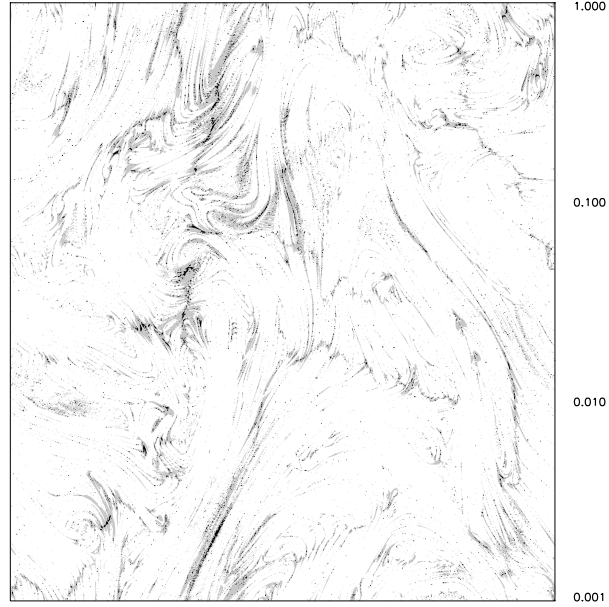
Fig. 4. Contour plots of the relative intensity of the neglected part of the nonlinear term $\mathrm{div}\,(\mathbf{u}'\omega')'$ compare to whole term $\mathrm{div}\,(\mathbf{u}\omega)'(\mathbf{x})$ in subfilter-scale equation: $\epsilon(\mathbf{x}) = |\mathrm{div}\,(\mathbf{u}'\omega')'(\mathbf{x})|/\{|\mathrm{div}\,(\mathbf{u}\omega)'(\mathbf{x})| + |\mathrm{div}\,(\mathbf{u}'\omega')'(\mathbf{x})|\}$. The relative contribution from the term $\mathrm{div}\,(\mathbf{u}'\omega')'$ is larger than 10% only in a very restricted location of the flow and is in most of the place smaller than 1%.

namics of the subfilter scales is the advection by the resolved scales. We therefore shall keep it exact in our numerical model. The term $\mathbf{U}\Omega$ is also important near the cut-off, because it acts as a "forcing" at the subfilter scales. Moreover, it includes only resolved fields and can be kept in numerical simulations at no additional cost. In what follows, we choose to neglect the two remaining terms: the term $u'\Omega$ is everywhere smaller by several orders of magnitude, and is always much less than the two other terms. Neglecting $u'\omega'$ term requires more justification since it becomes the second leading order term below half the cut-off scale. It appears however that his dynamical influence is negligible in 2D [11]. This has to be contrasted with the 3D case, where it acts as a turbulent viscosity and prevents small scale intermittent structures to grow unbounded [19]. This difference can probably be traced to the vortex stretching, which is absent in 2D.

2.3. The model

Keeping only the leading order contributions, the coupled equations (6) and (7) become

$$\partial_t \Omega + \mathrm{div}\,\overline{\mathbf{U}\Omega} + \mathrm{div}\,\overline{\mathbf{U}\omega'} = v\Delta\Omega, \tag{8}$$

$$\partial_t \omega' + \mathrm{div}\,(\mathbf{U}\omega') = F + (v + v_t)\Delta\omega',$$

$$F(\mathbf{x}, t) = -(\mathrm{div}\,(\mathbf{U}\Omega) - \mathrm{div}\,\overline{\mathbf{U}\Omega}) + \mathrm{div}\,\overline{\mathbf{U}\omega'}. \tag{9}$$

Here, v_t is a turbulent viscosity, which will be introduced to damp the small-scale noise arising in our numerical scheme and F is a force which describes the subfilter-scale generation via the enstrophy cascade (energy cascade in 3D).

3. Numerical implementation

3.1. Numerical strategy and performances

The resolved-scale equation has the form of Euler equation with an additional forcing coming from the interaction with the subfilter-scale motions. One is therefore led to standard strategies to solve this equation, depending on the type of the flow (spectral methods for flows in simple periodic geometry, or finite difference or finite elements for more complicated geometries). Here, we shall consider the periodic case, thereby using a spectral code for solving the resolved-scale equation. This code is described in [20].

The situation is markedly different at the subfilter level, where the basic equation is *linear* in the subfilter motions, with an inhomogeneous part provided by the subfilter-scale generation via the enstrophy cascade. This linearity suggests a solution strategy based on projection of the subfilter scales onto appropriate modes. Since the subfilter scales are usually very inhomogeneous and spatially intermittent, it seems logical to use a decomposition of the subfilter-scale velocity field into localized modes, thereby optimizing the memory requirements to store the subfilter-scale fields. A popular local mode decomposition uses wavelets (see e.g. [21]). Wavelets however would be difficult to implement in our method in which the wave packet size is fixed by the filtering scale and does not vary as in wavelets. Here, we choose to use a Gabor decomposition, which provides a fixed-size wave packet description and which allows theoretical manipulations similar to that obtained for Fourier modes. The linearity of the subfilter motions also provides room for a further computational time reduction via semi-Lagrangian methods of integration, using a time step related to the resolved scales. The numerical expected performances of our model, integrated using the semi-Lagrangian Gabor method at a given resolution and total integration time, are given in Table 1 and compared with both standard spectral methods based on FFT and FFT-based LES approaches. Computational time for several particular examples is given in Table 2 which shows an obvious gain in speed for our method with respect to the DNS.

Table 1
Comparison of estimated performance between DNS, classical turbulent models (like APVM or HDNS) based on FFT on a $(M \times M)$ grid and our model on a $(M \times M)$ grid for fully resolved scales and N_p modes for the subfilter-scale equation (see Section 3.5)

Model (resolution)	Integration time
DNS [FFT code] $(N \times N)$	$c_1 * N^2 \log(N)$
LES [FFT code] $(M \times M)$	$c_2 * M^2 \log(M)$
Our Model [FFT + Lagr.]	$c_3 * M^2 \log(M) + c_4 * N_p$

Table 2
Correlation between large-scale $(k < 21)$ vorticity from DNS and vorticity field from: our model with a maximum of 512^2 particles (M0 and M1) and 128^2 particles (M2), the APVM model and an hyperviscous simulation both on the resolved-scale grid $N = 64^2$

Model	$\tau = 15$	$\tau = 50$	Comp. time
DNS $(N = 1024)$	–	–	$\sim$10 days
M0 $(M = 64, N_p = 512^2)$	0.99403	0.89794	$\sim$1 h 30 min
M1 $(M = 64, N_p = 512^2)$	0.99450	0.82523	$\sim$1 h 30 min
M2 $(M = 64, N_p = 128^2)$	0.99409	0.89735	$\sim$8 min
APVM $(M = 64)$	0.95882	0.77429	$\sim$2 min
HDNS $(M = 64)$	0.93893	0.53231	$\sim$2 min

The same viscosity as in DNS was introduced in the resolved-scale equation for the M0 simulation whereas no viscosity was introduced for the M1 and M2 simulations. The correlation coefficient is given at two different times (15 and 50 turnover times). The computation times with a "Sun Ultrasparc 3000 workstation" are given in the last column.

If we now compare with the classical turbulent models, our method is somewhat slower because it is necessary to keep a sufficient number of localized modes for accurate description of the subfilter scales. However, a substantial gain in accuracy is achieved in comparison with traditional turbulent models because of the better description of the non-local interaction of scales.

3.2. Description of the algorithm

Implementation of our method consists of the following steps:
1. compute the force F (9) using the resolved and subfilter fields at time t;
2. project this force onto a set of Gabor modes;
3. advance the subfilter field to time $t + \mathrm{d}t$ in the Gabor space using a Lagrangian advection algorithm;
4. compute the resolved-velocity correlations at time $t + \mathrm{d}t$ using a procedure similar to the inverse Gabor transform;
5. advance the resolved-velocity field at time $t + \mathrm{d}t$ using the reconstruction of the "subfilter scale accelerator" (SFSA) (div $(\overline{\mathbf{U}\omega'})$).

Steps 1 and 5 involve standard procedures linked with our resolved-scale code (in the present case a Fourier spectral code with an Adams–Bashforth time stepping where a full dealiasing was introduced by keeping only the first 2/3 smaller wavenumbers in each direction, see [20]). Steps 2–4 involve new original procedures, based on interesting properties of the Gabor transform. For the sake of clarity, we present here only main results, leaving detailed computations in appendices.

3.3. The continuous Gabor transform

Here, we describe the wave packet description based on the Gabor transform which was introduced in [18] and further used in [13–15]. The Gabor transform (GT) is defined as

$$\widehat{\mathbf{u}'}(\mathbf{x}, \mathbf{k}, t) = \int f(\epsilon^*(\mathbf{x} - \mathbf{x}'))\mathrm{e}^{\mathrm{i}\mathbf{k}\cdot(\mathbf{x}-\mathbf{x}')}\mathbf{u}'(\mathbf{x}')\,\mathrm{d}\mathbf{x}', \tag{10}$$

where f is a rapidly decreasing function at infinity. Note that $1/\epsilon^*$ has a meaning of the scale separation length. It has to be chosen to lie in between of the integral scale and the Kolmogorov scale, the later being far in the subfilter range in many applications. For LES purposes, $1/\epsilon^*$ has to be close to (but not less than) the minimal resolved scale (grid scale $\mathrm{d}h$ in our case). Thus, to derive our model we need to assume the subfilter-scale wavenumber k to be greater than ϵ^* and use ϵ^*/k as a small parameter. This derivation will only be asymptotically exact when a spectral gap separating large and small scales is present. Otherwise, it will serve as a basis for an approximate numerical model, performance of which needs to be tested via comparison with DNS.

In the special case where $f = \sqrt{G}$, where G is the filter (see Eq. (3)), we have the following simple reconstruction formulae:

$$\mathbf{u}'(\mathbf{x}, t) = \frac{1}{(2\pi)^2 f(0)} \int \widehat{\mathbf{u}'}(\mathbf{x}, \mathbf{k}, t)\,\mathrm{d}\mathbf{k}, \tag{11}$$

$$\overline{\mathbf{U}\omega'}(\mathbf{x}, t) = \mathbf{U}\frac{1}{(2\pi)^2} \int \Re\left[\widehat{\omega'}(\mathbf{x}, \mathbf{k}, t)f(-\mathbf{k}, t)\right]\mathrm{d}\mathbf{k} + \mathrm{O}(\epsilon^*), \tag{12}$$

where $\Re$ means the real part, and finally [13]

$$\overline{u_i'u_j'}(\mathbf{x}, t) = \frac{1}{(2\pi)^2} \int \Re\left[\widehat{u_i'}(\mathbf{x}, \mathbf{k}, t)\widehat{u_j'}(\mathbf{x}, -\mathbf{k}, t)\right]\mathrm{d}\mathbf{k} + \mathrm{O}(\epsilon^*). \tag{13}$$

One may also note the connection between the Gabor velocity and the Gabor vorticity (similar to the Fourier quantities) [18]

$$\hat{\mathbf{u}}(\mathbf{k},t) = -\frac{i}{k^2}\hat{\omega}(\mathbf{k},t)(e_z \times \mathbf{k}) + O(\epsilon^*), \tag{14}$$

where e_z is a unit vector in z-direction.

Finally, one may show that the GT of the subfilter-scale equation (9) is (see Appendix A and [13,18] for more details)

$$(\partial_t + \mathbf{U} \cdot \nabla_x - \nabla_x(\mathbf{U} \cdot \mathbf{k}) \cdot \nabla_k)\widehat{\omega'}(\mathbf{x},\mathbf{k},t) \simeq \hat{F}(\mathbf{x},t) - (v + v_t)k^2\omega'(\mathbf{x},\mathbf{k},t). \tag{15}$$

3.4. Discrete optimal Gabor transform

Numerical implementation of the Gabor transform requires its discretization which will be presented in this section. Let us first of all note that the complete description of wave packets in the coordinate-wavenumber space may potentially require a number of modes which is much greater than in traditional spectral methods (up to N^{2D} versus N^D in D dimensions). However, this number can be greatly reduced if one is not interested if fair description of only the large scales and not fine details of the small-scale field. Moreover, even the small-scale fields are usually highly intermittent in the Gabor (or wavelet) space and may be represented with a high precision by a small set of Gabor modes, potentially even smaller than N^D (see e.g. [22]). The algorithm we devised uses N^D Gabor modes and therefore there is a room for further code optimization.

3.4.1. The discretization

The discretization of the subfilter field in the Gabor space is done via a particle in cell (PIC) method. This method is traditionally used in plasma physics, but was used previously in hydrodynamics by Nazarenko et al. [23] to study the interaction of sound wave packets with turbulence. Details about the method can also be found in [10]. In this method, the Gabor modes of the subfilter-scale vorticity field are replaced with discrete wave packets (particles). To avoid confusion, we emphasize the difference between PIC and the vortex-in-cell method: the former provides information about the subfilter scales via the wavenumber distribution whereas the later does not contain any of such information because vortices (unlike wave packets) do not possess any fine subgrid structure. Let us consider discretization of the vorticity field $\widehat{\omega'}(\mathbf{x},\mathbf{k},t)$ by $2N_p$ wave packets in the Gabor space

$$\widehat{\omega'}(\mathbf{x},\mathbf{k},t) = \sum_{\alpha=1}^{2N_p} \hat{\sigma}_\alpha(t)S_{\mathbf{x}}(\mathbf{x} - \mathbf{x}_\alpha(t))S_{\mathbf{k}}(\mathbf{k} - \mathbf{k}_\alpha(t)). \tag{16}$$

In (16), α labels the wave packet. Note that our representation allows several wave packets with different wavenumbers to be located at the same position $\mathbf{x}$, like in the Gabor transform. Here, $S_{\mathbf{x}}$ and $S_{\mathbf{k}}$ are some interpolating functions (particle "size"). Since the computation of non-linear terms in the resolved-scale equation involves a first-order spatial derivative, we are led to choose a linear interpolation in the $\mathbf{x}$-direction. In the $\mathbf{k}$-direction, a zero particle "thickness" turns out to be sufficient for our purpose. We thus adopt the following representation:

$$S_{\mathbf{x}}(\mathbf{x}) = S(x)S(y), \tag{17}$$
$$S_{\mathbf{k}}(\mathbf{k}) = \delta(p)\delta(q), \tag{18}$$

where $\mathbf{x} = (x,y)$, $\mathbf{k} = (p,q)$, δ is the Dirac function and the function $S(\eta)$ is defined by

$$S(\eta) = \begin{cases} (dh - |\eta|)/dh & \text{if } |\eta| < dh, \\ 0 & \text{otherwise.} \end{cases} \tag{19}$$

Here, dh is a length scale governing the accuracy of the discretization. Its choice will be discussed later on.

The PIC algorithm of reconstruction of the continuous fields from the discretized coefficients provides a natural filter G and the function f to be used in the Gabor transform through (see Appendix D)

$$G(\mathbf{x}) = f^2(\mathbf{x}) = f^2(0) \times S_{\mathbf{x}}^2(\mathbf{x}) \tag{20}$$

with

$$f(0) = \frac{1}{\sqrt{\int S_{\mathbf{x}}^2(\mathbf{x}') \, d\mathbf{x}'}}. \tag{21}$$

In the $\mathbf{k}$ space, the filtering operation is achieved by simply multiplication of the Fourier coefficients by the Fourier transform of G, which is

$$\hat{G}(p,q) = \frac{36}{(p \, dh)^2 (q \, dh)^2} \left\{ \left(1 - \frac{\sin(p \, dh)}{p \, dh} \right) \left(1 - \frac{\sin(q \, dh)}{q \, dh} \right) \right\}. \tag{22}$$

3.4.2. Reconstruction of the subfilter-scale correlations

With our discretization, the formulae of reconstruction of the subfilter correlations (12) can be obtained using (16). Taking into account that ω' is real, we have (see Appendix C for details)

$$\overline{\mathbf{U}\omega'}(\mathbf{x}, t) \simeq 2\mathbf{U} \sum_{\alpha_+=1}^{N_p} \Re\left[\widehat{\sigma_{\alpha_+} f^*}(\mathbf{k}_{\alpha_+}) \right] S_{\mathbf{x}}(\mathbf{x} - \mathbf{x}_{\alpha_+}), \tag{23}$$

where the sum is only over the wave packets with positive wavenumbers p_α. [1] Similarly, one can use (B.2) and (16) to re-write (13) as (C.10) (see Appendix C)

$$\overline{u'v'}(\mathbf{x}, t) \simeq 2 \sum_{\alpha_+=1}^{N_p} \frac{-q_{\alpha_+} p_{\alpha_+}}{(p_{\alpha_+}^2 + q_{\alpha_+}^2)^2} |\hat{\sigma}_{\alpha_+}|^2 S_{\mathbf{x}}^2(\mathbf{x} - \mathbf{x}_{\alpha_+}),$$

$$\overline{u'^2}(\mathbf{x}, t) \simeq 2 \sum_{\alpha_+=1}^{N_p} \frac{+q_{\alpha_+}^2}{(p_{\alpha_+}^2 + q_{\alpha_+}^2)^2} |\hat{\sigma}_{\alpha_+}|^2 S_{\mathbf{x}}^2(\mathbf{x} - \mathbf{x}_{\alpha_+}), \tag{24}$$

$$\overline{v'^2}(\mathbf{x}, t) \simeq 2 \sum_{\alpha_+=1}^{N_p} \frac{+p_{\alpha_+}^2}{(p_{\alpha_+}^2 + q_{\alpha_+}^2)^2} |\hat{\sigma}_{\alpha_+}|^2 S_{\mathbf{x}}^2(\mathbf{x} - \mathbf{x}_{\alpha_+}).$$

3.4.3. Particle discretization of the small-scale field

Let us consider a small-scale vorticity field $\omega'(\mathbf{x}, t)$ and represent it as a sum of discrete Gabor modes as follows:

$$\omega'(\mathbf{x}, t) = \frac{2}{f(0)} \sum_{\alpha_+=1}^{N_p} \Re\left[\sigma_{\alpha_+} \right] S_{\mathbf{x}}(\mathbf{x} - \mathbf{x}_\alpha). \tag{25}$$

---

[1] Since the vorticity $\omega'(\mathbf{x}, t)$ is real, each wave packet at position $\mathbf{x}_\alpha$ and with wavenumber $\mathbf{k}_\alpha$ will have a partner wave packet with same amplitude, at the same location and with an opposite wavenumber $-\mathbf{k}_\alpha$.

An easy way to satisfy (25) exactly is to create one wave packet at each grid point, so that $N_p = N^2$ (i.e. N^2 Gabor modes, for a N^2 initial discrete field). This is the simplest discretization but it could easily be modified according to a specific problem requirements. Applying Eq. (25) at each grid point $\mathbf{x}_i$, we then obtain

$$\omega'(\mathbf{x}_i, t) = \frac{2}{f(0)} \Re[\sigma_{\alpha_i}]. \tag{26}$$

This equation fixes the real part of the wave packet amplitude σ_{α_i} and its coordinates $\mathbf{x}_{\alpha_i}$. Let us now use the velocity at the grid point $u'(\mathbf{x}_i)$ to find the further two conditions:

$$u'(\mathbf{x}_i, t) = \frac{2}{f(0)} \frac{-q_{\alpha_i}}{(p_{\alpha_i}^2 + q_{\alpha_i}^2)} \Im[\sigma_{\alpha_i}], \tag{27}$$

$$v'(\mathbf{x}_i, t) = \frac{2}{f(0)} \frac{+p_{\alpha_i}}{(p_{\alpha_i}^2 + q_{\alpha_i}^2)} \Im[\sigma_{\alpha_i}]. \tag{28}$$

These conditions link the two components of the wavenumber with the imaginary part of the wave packet amplitude, which is still a free parameter at this stage. We then select the phase of the GT by requiring that the imaginary part of the wave packet equals its real part. Other choices have been tried and the results turned out to be not sensitive to the initial phase. The initial values for each wave packets α_i can finally be summarized as

$$\begin{cases} \Re[\sigma_{\alpha_i}] = f(0)\omega'_f(\mathbf{x}_i)/2, \\ \Im[\sigma_{\alpha_i}] = \Re[\sigma_{\alpha_i}], \\ q_{\alpha_i}/p_{\alpha_i} = -u'_f(\mathbf{x}_i)/v'_f(\mathbf{x}_i), \\ p_{\alpha_i} = \frac{\omega'_f(\mathbf{x}_i)\left(q_{\alpha_i}/p_{\alpha_i}\right)^2}{v'_f(\mathbf{x}_i)(1+\left(q_{\alpha_i}/p_{\alpha_i}\right)^2)}, \\ \mathbf{x}_{\alpha_i} = \mathbf{x}_i. \end{cases} \tag{29}$$

This procedure creates N^2 wave packets from any vorticity field on a grid of size $2\pi/N$ and can be used to initialize the subfilter-scale vorticity field from any given initial condition or a force F by transforming it into an equivalent vorticity field $\omega'_f(\mathbf{x}, t) = F(\mathbf{x}, t)\, dt$.

3.5. The Lagrangian scheme

A Lagrangian interpretation of the subfilter-scale equation (15) shows that its time integration is equivalent to the motion of wave packets in the $(\mathbf{x}, \mathbf{k})$ space. Each wave packet carries a complex amount of Gabor vorticity (σ_α) and is advected by the resolved-scale velocity $\mathbf{U}(\mathbf{x})$, while its wavenumber and amplitude evolve according to the local resolved velocity gradient. For the trajectory of the wave packet and its amplitude we have

$$\dot{\mathbf{x}}_\alpha = \mathbf{U}(\mathbf{x}_\alpha(t)), \tag{30}$$

$$\dot{\mathbf{k}}_\alpha = -\nabla_x(\mathbf{k}_\alpha(t) \cdot \mathbf{U}(\mathbf{x}_\alpha(t))), \tag{31}$$

$$\dot{\sigma}_\alpha = \hat{F}(\mathbf{x}_\alpha, \mathbf{k}_\alpha, t) - (v + v_t)k_\alpha^2 \sigma_\alpha. \tag{32}$$

By these equations, the wave packets move continuously in the physical space in between the grid points, i.e. they are not constrained by the resolution associated with the spectral part of the code. To find the resolved-scale quantities at the position of each particle (i.e. possibly in between grid mesh points), an interpolation procedure is used via the functions $S_{\mathbf{x}}$ and $S_{\mathbf{k}}$ associated with the PIC method.

3.6. Initial conditions

All the simulations used the same initial random vorticity field with all the energy concentrated at very large scales (the initial energy spectrum is given by $E(k) = k\mathrm{e}^{-(k-k_0)^2}$ with $k_0 = 1$). In practice, the noise associated with the PIC method is a function of the number of wave packets used for computation. If the initial condition is such that the initial grid on which the vorticity is defined is too coarse (M too small), one can use a two step procedure to reach a reasonable number of wave packets: in a first stage of the simulation, we create at each time step M^2 wave packets with the vorticity $\omega_f'(\mathbf{x}, t) = F(\mathbf{x}, t)\,\mathrm{d}t$ created by the forcing F. During this stage, the wave packets which were created at earlier times are moved into the phase space using the ray equations (30) and (31), but their amplitude is kept constant. This procedure is used until the total number of wave packet reaches a desired number. From this point on, the wave packet creation is shut down, and the wave packets are evolved according to (30)–(32).

3.7. Noise reduction and effective turbulent viscosity

The PIC method induces a numerical noise at very small scales, which is a function both of the integration time and the total number of particles. We have found that an efficient way to reduce this subfilter-scale noise could be achieved by periodically recreating a new set of N_p wave packets via first a rebuilding of the vorticity field in the physical space, on a grid of size $\sqrt{N_p}$ using (11), followed by a re-creation of wave packets using (29). This procedure keeps the correlations associated with the subfilter-scale field unchanged, and therefore does not affect directly the resolved scale. In effect, this procedure acts as a filter for the subfilter scales which are smaller than the size of the reconstruction grid, and thus, can be seen as an effective turbulent viscosity, which cannot be estimated a priori but which adjusts itself to the noise level.

3.8. Test of the accuracy of the method

To test the accuracy of our numerical method, we have performed a priori tests using data from a DNS at high resolution. The total vorticity field was divided into a subfilter- and a resolved-scale fields using the same filter as in our model. The subfilter-scale field is further discretized into wave packets according to Eq. (29). A comparison was then made between the various components of the stresses in the DNS, and in our discretization scheme. Fig. 5 shows the results for the square modulus of each of the three Reynolds stress components with respect to their wavenumbers. The accuracy of the discretized reconstruction of each term is remarkable for the large scales. At very small scales ($k > 42$), the discretization tends to produce noise in the components of the SFSA involving the subfilter-scale velocity. In our case, we do not consider these terms so that we do not have to bother about this noise. In situations where such troublesome terms are considered, the noise can be removed via a filtering at small scale. In spectral simulations, this truncation is provided naturally via the dealiasing procedure which filters out modes larger than $2k_{\max}/3$, where $k_{\max}$ is the maximum wavenumber of the resolved-scale field.

The inset of Fig. 5 shows the comparison between the true velocity correlations versus the PIC-modeled SFSA after dealiasing. The agreement is nearly perfect.

4. Numerical results

Our method can be used to perform two kind of simulations, depending on whether one is interested in the small-scale behavior or not. In the first case, one needs to model the subfilter scales with a large number of wave packets, so as to be able to reconstruct the small-scale field with a good accuracy. In extreme cases, one needs about $N_p = N^2$ wave packets to be able to reconstruct faithfully details at scale $2\pi/N$ and to
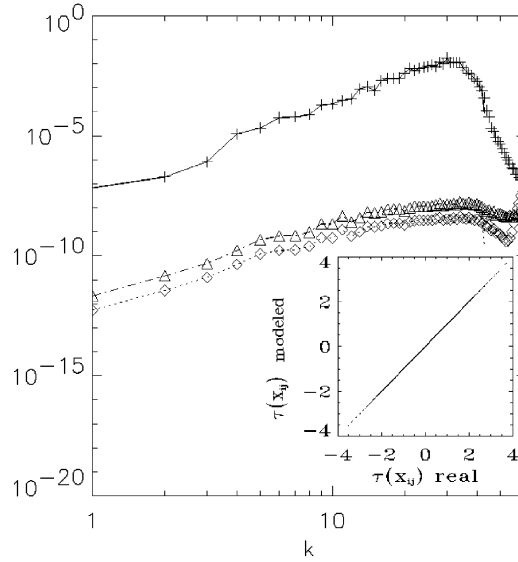
Fig. 5. Moduli of the three non-linear terms in the resolved-scale equation (6) computed directly by the spectral method (lines) compared with the same fields rebuilt by the PIC method (symbols). Here, + and – are used for the field $|\mathrm{div}\,\overline{(\mathbf{U}\omega')}(k)|^2$, $\triangle$ and $-\cdot-$ for $|\mathrm{div}\,\overline{(\mathbf{u}'\omega')}(k)|^2$ and $\Diamond$ and $---$ for $|\mathrm{div}\,\overline{(\mathbf{u}'\Omega)}(k)|^2$. Corresponding comparison of the true and the PIC-modeled velocity correlations $\tau = \mathrm{div}\,(\overline{\mathbf{u}\omega}) - \mathrm{div}\,(\overline{\mathbf{U}\Omega})$ at each grid point X_{ij} is shown in inset.

produce the same amount of information as a direct numerical simulation at resolution N^2. As we mentioned before however some of modes will typically have negligible amplitudes in the Gabor space and a fairly detailed description of small scales can be achieved with N_p considerably less than N^2. In the case when only large scales matter, one needs to keep the smallest number of wave packet necessary to compute accurately the velocity correlations at the wavenumber cut-off. Since the resolved-scale field at the cut-off $k_c = M/2$ produces (by non-linear beating) information up to scale $2\pi/M$, we used a minimum of $N_p = M^2$ wave packets in our "large eddy simulations". Finally, note that our method allows nearly inviscid computations, since it does not require the existence of a viscosity at large scale and since it uses a minimal "effective viscosity" which starts acting only at scales $2\pi/M$. Very large Reynolds number can then be achieved via an adequate number of wave packets.

We present results illustrating these points in two classical situations – decaying and forced turbulence. In each case, the performance of our model is discussed and compared with results from the DNS and other popular subfilter-scale parameterizations used in 2D turbulence.

4.1. Decaying turbulence

For the decaying case, the initial condition was chosen so that the energy is concentrated at very large scales. The reference DNS was performed at a resolution $N^2 = 1024^2$ with a viscosity $v = 1.8 \times 10^{-4}$, leading to a Reynolds number $Re \sim 10^4$ (based on the integral scale and the RMS velocity). The simulation was stopped after approximately 50 turnover times, by which time the initial condition has evolved into a robust dipole structure. The separation between resolved and subfilter scales used for our model is taken at $k_c = 21$, corresponding to a computation over a grid 64^2.

Let us first compare the DNS to our model using a large number of wave packets ($N_p = 512^2$). We ran a simulations with the same viscosity v at large scales and no viscosity at small scales. (run M0 in Table 2).

The total simulation time is about 1h30 on a Sun workstation, roughly 150 times less than the DNS. The total vorticity field after 50 turnover times, reconstructed by adding the contributions from the resolved and subfilter scales, is shown in Fig. 6 and compared with the vorticity field of the DNS. A global comparison for small and large scales can also be done via the energy spectra, see Fig. 7.

Clearly, the two pictures display good overall similarities at large scales, and marked differences at smaller scales. The largest structures are very similar and they are well localized even after 50 turnover times. The spectra in the two simulations overlap. We also performed a model simulation with the same parameters as in M0 but without viscosity (run M1). We observed that such a model gives poorer
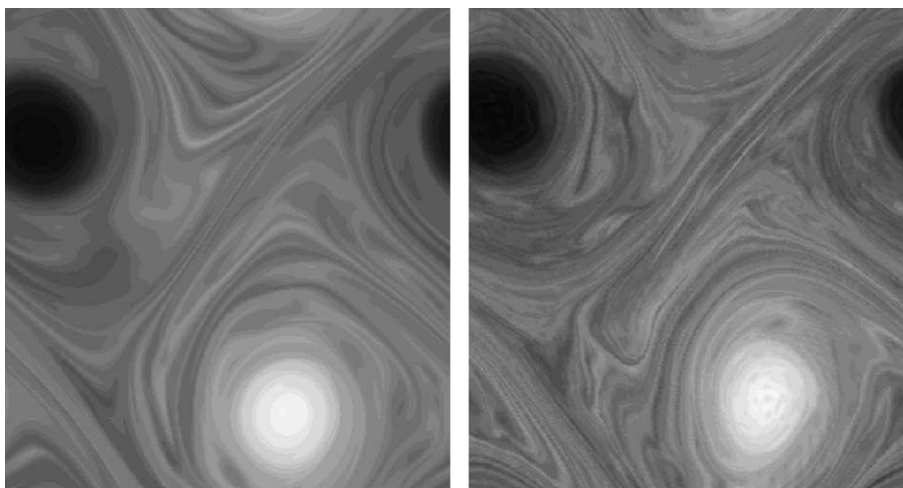

Fig. 6. Total vorticity field of decaying turbulence after 50 turnover times as computed by DNS on a 1024^2 grid with viscosity $v = 1.8 \times 10^{-4}$ (left) compared with the same field computed by the model M0 described in Table 2 (right).
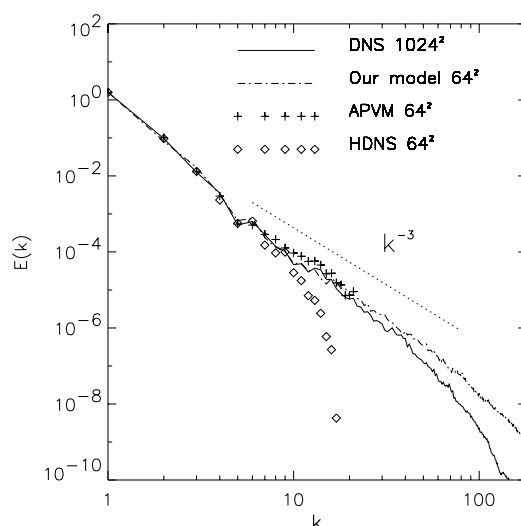

Fig. 7. The energy spectra obtained by the same simulation as in Fig. 2 compared with the spectra obtained by some other methods including our model with parameters M0 from Table 2.
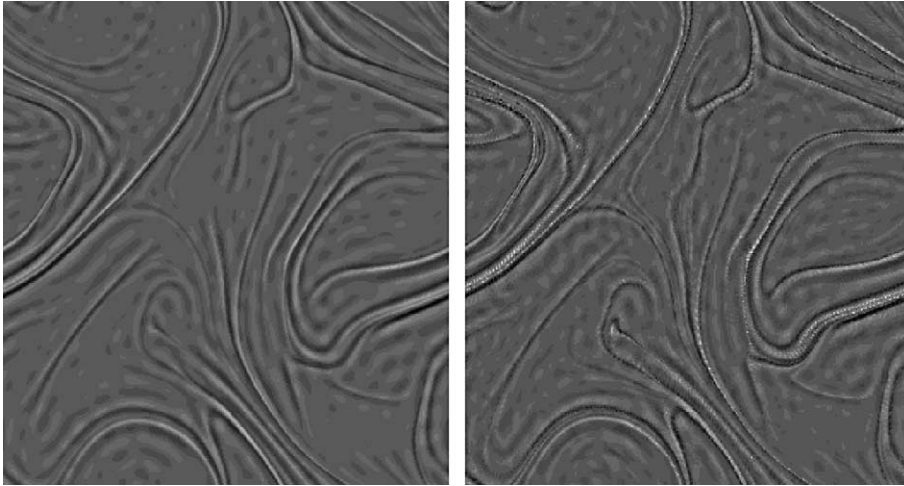
Fig. 8. Small-scale vorticity field of decaying turbulence after 15 turnovers. Result from a DNS on a 1024^2 grid with $v = 1.8 \times 10^{-4}$ (left) and from our model (M0).

agreement of the large-scale structures with the (viscous) DNS than model M0 does, which is natural because the viscous effects are taken into account in M1 at least in the large scales. On the other hand, it may seem inconsistent that we ignored viscosity in the subfilter component while leaving it in the resolved (large-scale) component. Technically, computing inviscid subfilter scales is much faster because one does not need to compute the wave packet wavenumbers in this case. The reason why this makes sense however is that the subfilter scales appear to affect the large-scale dynamics mainly via allowing the enstrophy transfer through the cut-off wavenumber and thereby preventing the spectrum pile-up near the smallest resolved scale. Such an enstrophy transfer is provided via the largest of the subfilter scales where the viscous effects have not had enough time to be seen. Together, these results confirm that at large scales, the dynamically important coupling term between resolved and subfilter scales is the term $\mathrm{div}\,(\overline{U}\omega')$, in agreement with the analysis of Laval et al. [11]. At small scales, model M0 seems to produce thinner filaments and smaller structures than in the DNS. This effect is clearly visible on the spectra of the two simulations: in the DNS, the k^{-3} inertial law starts to level off towards $k = 60$ (due to viscous effects), while in our model, the power law extends over a wider range of scales, up to approximately $k = 100$. To check whether this difference comes from our subfilter scale scheme, we performed a direct comparison of the smallest scales of the simulation $k > 21$. Fig. 8 shows such a comparison at some earlier time (after about 15 turnover times), when the small scales have not yet been washed out by viscosity.

At this time, differences are negligible, proving that our model also captures the dominant coupling mechanism at subfilter scales. This finding is also in agreement with the dynamical analysis of Laval et al. [11]. The further differences arising over longer time scales can therefore be due to two effects: one is the error accumulation due to sub-dominant neglected terms in our model (like the terms involving coupling of the resolved vorticity Ω with the subfilter velocity $\mathbf{u}'$); the second is viscous effects. We believe that the first possibility is ruled out by the analysis of Laval et al. [11], in which numerical simulations of our model equations were performed using the same viscosity as in the direct numerical simulations. [2] In that case, the differences at small scales appear to be negligible. We therefore interpret the differences between the two

---

[2] These simulations were not fast: they were based on spectral methods and were slower than the direct method.

models as a viscous effect, and, actually, as an indication of the lower effective dissipation in our model. This explains both the later bending of the spectra, and the finer structure of the filaments.

Finally, we performed a third run using the minimum number of wave packets equal, in the present case, to $N_p = 128^2$ (run M2 in Table 2). In this case, the number of wave packets does not allow accurate reconstruction for the scales less than $2\pi/128$. The simulation is however much faster, and takes only 8 min of computational time. The total large-scale vorticity field after 50 turnover times is compared with the corresponding large-scale vorticity field of the DNS in Fig. 9.

The agreement is still very good. To quantify deviations of the large-scale structures in all three model runs (M0, M1 and M2) and DNS, we computed the correlation coefficient between two simulations defined by
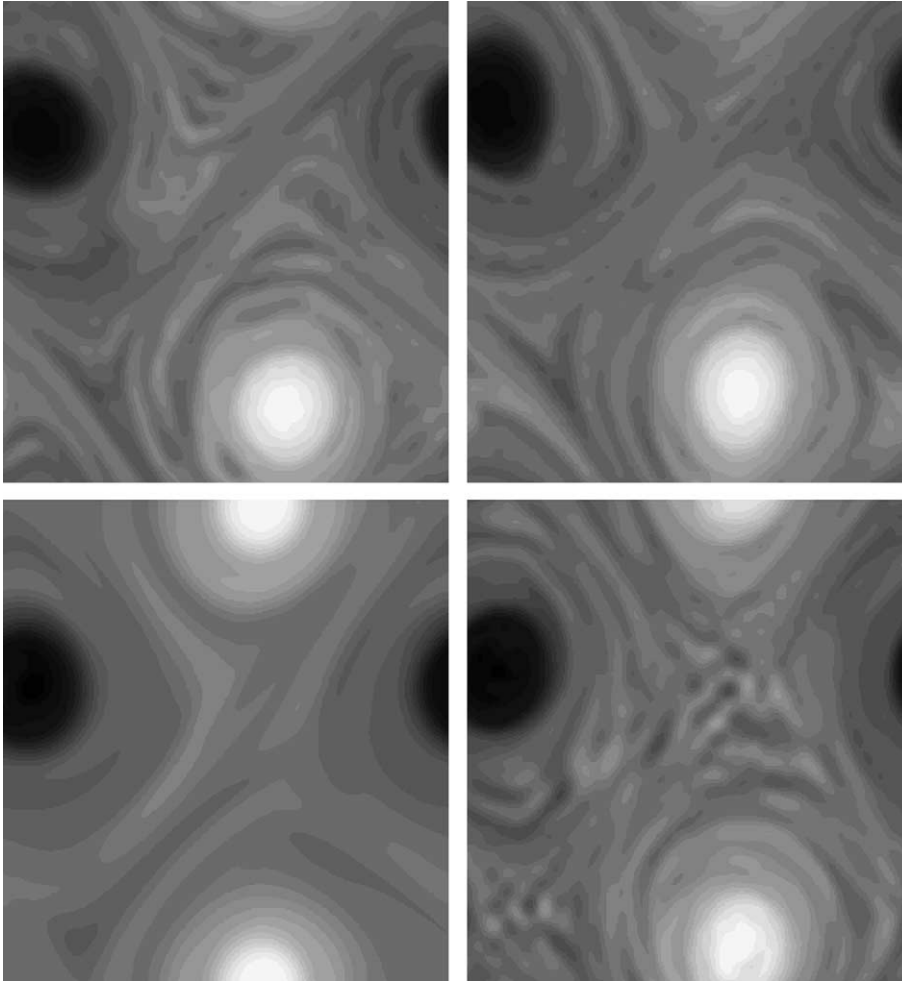

Fig. 9. Large-scale vorticity field ($k \leqslant 21$) after 50 turnover times in decaying turbulence. (upper left) DNS on a 1024^2 grid and $v = 1.8 \times 10^{-4}$, (upper right) our model (M2 in Table 2) with a separation scale at $k = 21$ and 16,384 modes in subfilter scales, (lower left) simulation with hyperviscosity (using $v_p k^p \omega$ as the dissipation term with $p = 8$) on a 64^2 grid and (lower right) simulation with the APVM model [24] on a 64^2 grid.

$$C_{1,2} = \frac{\sum_{1<i,j<64} \omega_1(i,j)\omega_2(i,j)}{\sqrt{\sum_{1<i,j<64} \omega_1(i,j)^2 \sum_{1<i,j<64} \omega_1(i,j)^2}}, \tag{33}$$

where $\omega_1(i,j)$ and $\omega_2(i,j)$ are the large-scale vorticity fields computed with two different methods. This correlation coefficient was computed at two times corresponding to 15 and 50 turnover times and is reported in Table 2. At earlier time, our three models (viscous or not) are all characterized by a very good correlation coefficient (about 99%). At later time, slight differences appear. In fact, the best correlations are achieved by the viscous model, and the model with the least number of subgrid-scale modes. This is not surprising, since our noise removing procedure produces an effective viscosity which is larger as the number of subgrid-scale modes decreases. The high resolution model M1 is then the less viscous model of all three and therefore can be expected to produces the largest difference with respect to the viscous DNS. The correlation of the simulation M2 with respect to the DNS show that the dissipation effect of the regeneration procedure of small scales seems to have a similar effect as the explicit dissipation introduced in the simulation M0 as it leads to the same correlation coefficient after 50 turnover times.

Two other popular 2D turbulent models were also tested along the same line. In the first one (HDNS), the viscous term $v\Delta\Omega$ of the Navier–Stokes equation is replaced by a "hyperviscous" term $v_p\Delta^p\Omega$. In our simulations, we took $p = 8$ and $v_p = 10^{-18}$. The use of such a large-p hyperviscosity is common in simulations of 2D turbulence [25–27]. The hyperviscosity can lead to spurous effects [28] but is an efficient model for the simulation of high Reynold number flows at low resolution. The second model is the anticipated potential vorticity model (APVM) developed by Sadourny and Basdevant [24]. Both models are very cheap, taking only about 2 min of computational time. They are also less accurate, as can be seen from both Fig. 9, and Table 2. In the HDNS 64^2, the correlation coefficient is only about 50% in the end of the simulation. For the APVM, it is higher (about 75%), but still lower than our "minimal model" M2. The energy spectra of the 4 simulations can also be compared, see Fig. 7. Our model develops an energy spectrum very close to the APVM one, and slightly less steep than the DNS at scales close to the cut-off. This is because at this scale, viscous effects start being felt and tend to bend the spectrum. The HDNS spectrum is much steeper near the cut-off than both the reference DNS and the two other models.

4.2. Forced turbulence

Similar simulations were performed in the case of forced turbulence. In such a case, our model was ran with $M^2 = 64^2$ resolved-scale Fourier modes, and $N_p = 512^2$ subfilter-scale Gabor modes, and no viscosity at small scales. Runs were also performed using HDNS and APVM models over 64^2 Fourier modes. The initial condition is a vorticity field with an energy spectrum concentrated at the forced wavenumber ($k = 15$) and with a small amount of total energy. The simulation was forced by keeping constant the energy of the mode $\mathbf{k} = (15,0)$. In this situation, the vorticity field is progressively built via the stochastic forcing (which is itself strongly dependent on the exact structure of the vorticity field since it must aim at keeping one mode constant). Due to the developing spectral cascades, the scale interactions become more local and we may then expect the sub-dominant terms to play an enhanced role (with respect to the decaying case). Indeed, we have observed that the vorticity fields in the DNS and in the model do not exactly coincide: both simulations display similar small scale intense vortices, but they are not located at the same places. This effect can also be seen more clearly in the spectra, see Fig. 10. Due to the chaoticity, they all differ at the mode $k = 1$ which is the most sensitive to the exact position of each individual vortex. At smaller scales, marked differences appear between the models. Clearly, the HDNS gives the worst result, with a large deficit of energy over all scales. This is because in this case, the forcing scale is very close to the scale at which the dissipation takes place, and most of the energy is dissipated before the inverse cascade to larger scales can occur. The two other models, which do not introduce an explicit dissipation at the cut-off
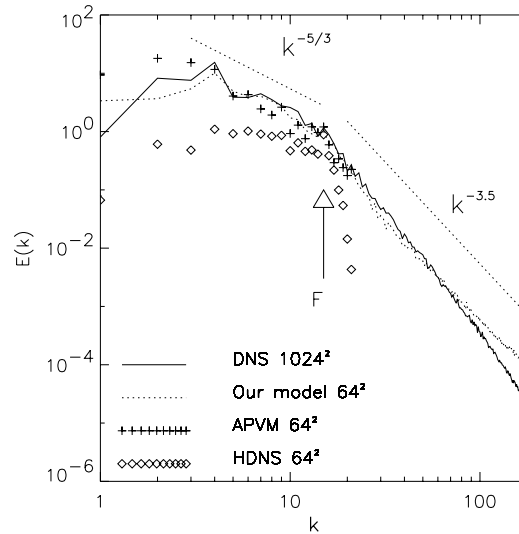
Fig. 10. Comparison of the energy spectra of forced turbulence after 150 turnover times computed by different methods (our model refers to the run M0 from Table 2).

scale, perform much better. The APVM model tends to overestimate the rate of energy at the largest scale and to underestimate it in the inertial range. Our model slightly underestimates the amount of energy at the largest scale, but gives results very close to the DNS in the inertial range of scale. At scales smaller than the cut-off, both the DNS and our model produce an energy spectra steeper than the k^{-3} law. At the largest wavenumber, the beginning of the viscous range is clearly visible in the DNS but not in our model. This is again an indication of the large Reynolds number achieved by our model. As for computational times, the performances are similar to the decaying case.

5. Discussion

We developed a new dynamic model of subfilter-scale turbulence based on a simple hypothesis about the subfilter-scale evolution. This approach is different from traditional turbulent models since our model provides expressions of the turbulent Reynolds subgrid stresses via estimates of the subgrid velocities rather than velocities correlations. The subfilter-scale dynamic is given by a linear equation, describing the advection of subfilter-scale wave packets with the mean flow. This feature allows a reduction of the time step used in the simulation, via the use of a pseudo-Lagrangian method. We thereby have achieved a reduction of the computational time by a factor 150 in the typical cases we considered. Our method can also be used for large eddy simulation strategies, in which only the large scales are computed. This allows a large memory savings, and an additional reduction of the computational time (typically a factor 100 in the case we considered). The resulting simulation is more costly than a traditional LES simulation, based on fast Fourier transform algorithms (like hyperviscosity or vorticity dissipative schemes). It could however become more competitive for more complicated geometries, where finite difference schemes become more appropriate than FFT. This would make LES models based on hyperviscous schemes much more costly, while our method would proportionally keep at the same computational performance.

In the present paper, only 2D turbulence has been considered. As is well known, 2D turbulence is very special because there is no vortex stretching. One may therefore wonder whether our model could be

applied to 3D flows. To answer this question, Laval et al. [12] have recently performed a numerical analysis of the hypotheses pertaining our turbulent model. The main hypothesis is that the subfilter dynamics can be very well approximated by an equation in which non-local terms are retained, while local terms (non-linear in the subfilter velocities) are replaced by a turbulent viscosity. The numerical analysis performed via a numerical simulation of the coupled resolved and approximate subfilter equations indeed showed that such hypothesis is valid, insofar as both the energy spectra, the structures and the statistical properties of such a model were very close to that of a DNS. Even though this analysis can only be performed at a rather moderate Reynolds number (80–200, based on the Taylor scale), we find this analysis encouraging.

Finally, we would like to mention that the proposed approach is likely efficient for LES modelling of MHD fluids. Indeed, a typical feature of many magnetized flows is presence of a large-scale magnetic field which reinforces the non-locality of the scale interactions. Of course, the method will have to be significantly modified in this case to take into account the Alfven waves which arise at small scales when a large-scale magnetic field is present.

Appendix A. Derivation of the subfilter-scale equation in (x,k) space

Some properties of the GT will be useful in the paper. They are (see [13,15] for details)

$$\widehat{\partial_i \mathbf{u}'}(\mathbf{x}, \mathbf{k}, t) = \partial_i \widehat{\mathbf{u}'}(\mathbf{x}, \mathbf{k}, t), \tag{A.1}$$

$$= i k_i \widehat{\mathbf{u}'}(\mathbf{x}, \mathbf{k}, t) + \mathrm{O}(\epsilon^*), \tag{A.2}$$

$$\widehat{\mathbf{U}\omega'}(\mathbf{x}, \mathbf{k}, t) \simeq \mathbf{U}(\mathbf{x}, t)\widehat{\omega'}(\mathbf{x}, \mathbf{k}, t) + i(\nabla_x \cdot \nabla_k)\mathbf{U}\omega'. \tag{A.3}$$

Let us derive the GT of the equation

$$\partial_t \omega' + \mathrm{div}\,(U_j \omega') = F(\mathbf{x}, t) + (v + v_t)\Delta\omega'. \tag{A.4}$$

Using (A.2), we find that the GT of the viscous term is $-(v + v_t)k^2\widehat{\omega'}$. The GT and the time derivative commute, so that the GT of the first term of the l.h.s. gives

$$\widehat{\partial_t \omega'} = \partial_t\,\widehat{\omega'} \tag{A.5}$$

Using the space derivative property (A.2), the GT of the second terms can be developed into

$$\widehat{\partial_j U_j \omega'} = \widehat{U_j \partial_j \omega'} \simeq U_j \widehat{\partial_j \omega'} + i\partial_l U_j \frac{\partial}{\partial k_l}\widehat{\partial_j \omega'} \simeq U_j \partial_j \widehat{\omega'} + i\partial_l U_j \frac{\partial}{\partial k_l}\left(ik_j \widehat{\omega'}\right)$$

$$\simeq U_j \partial_j \widehat{\omega'} + i\partial_l U_j k_j \frac{\partial}{\partial k_l}\widehat{\omega'} - \widehat{\omega'}\partial_j U_j \tag{A.6}$$

Using the incompressibility ($\partial_j U_j = 0$), we finally obtain

$$D_t \widehat{\omega'}(\mathbf{x}, \mathbf{k}, t) \simeq \hat{F}(\mathbf{x}, t) - (v + v_t)k^2\widehat{\omega'}(\mathbf{x}, \mathbf{k}, t) \tag{A.7}$$

with

$$D_t = \partial_t + \mathbf{U} \cdot \nabla - \nabla_x(\mathbf{U} \cdot \mathbf{k}) \cdot \nabla_k. \tag{A.8}$$

Appendix B. Reconstruction formulae for the correlations

Using the formula (A.2) for the GT of space derivative, one can derive the subfilter-scale velocity field in the $(\mathbf{x},\mathbf{k})$ space with respect to the subfilter-scale vorticity

$$
\widehat{\omega'}(x,y,p,q,t) = \widehat{\partial_x v'}(x,y,p,q,t) - \widehat{\partial_y u'}(x,y,p,q,t) = \partial_x \widehat{v'}(x,y,p,q,t) - \partial_y \widehat{u'}(x,y,p,q,t)
$$
$$
= \mathrm{i}p\widehat{v'}(x,y,p,q,t) - \mathrm{i}q\widehat{u'}(x,y,p,q,t) + \mathrm{O}(\epsilon^\star), \tag{B.1}
$$

where $\mathbf{k} = (p,q)$ and $\mathbf{x} = (x,y)$. Reversing the formula, we obtain the expression of the Gabor transform of the velocity

$$
\widehat{u'}(x,y,p,q,t) = \frac{\mathrm{i}q}{p^2 + q^2}\widehat{\omega'}(x,y,p,q,t) + \mathrm{O}(\epsilon^\star), \tag{B.2}
$$

$$
\widehat{v'}(x,y,p,q,t) = \frac{-\mathrm{i}p}{p^2 + q^2}\widehat{\omega'}(x,y,p,q,t) + \mathrm{O}(\epsilon^\star). \tag{B.3}
$$

Consider now the following expression:

$$
\int \frac{1}{2}\left[\widehat{u'}(\mathbf{x},\mathbf{k},t)\widehat{\omega'}(\mathbf{x},-\mathbf{k},t) + \widehat{u'}(\mathbf{x},-\mathbf{k},t)\widehat{\omega'}(\mathbf{x},\mathbf{k},t)\right]\mathrm{d}\mathbf{k} = \int \Re\left[\widehat{u'}(\mathbf{x},\mathbf{k},t)\widehat{\omega'}(\mathbf{x},-\mathbf{k},t)\right]\mathrm{d}\mathbf{k}
$$
$$
= \int \Re\left[\int f(\epsilon^\star(\mathbf{x}-\mathbf{x}'))\mathrm{e}^{\mathrm{i}\mathbf{k}(\mathbf{x}-\mathbf{x}')}u'(\mathbf{x}',t)\,\mathrm{d}\mathbf{x}' \int f(\epsilon^\star(\mathbf{x}-\mathbf{x}''))\mathrm{e}^{\mathrm{i}\mathbf{k}(\mathbf{x}-\mathbf{x}'')}\omega'(\mathbf{x}'',t)\,\mathrm{d}\mathbf{x}''\right]\mathrm{d}\mathbf{k}
$$
$$
= \int f(\epsilon^\star(\mathbf{x}-\mathbf{x}'))f(\epsilon^\star(\mathbf{x}-\mathbf{x}''))u'(\mathbf{x}',t)\omega'(\mathbf{x}'',t)\left(\int \mathrm{e}^{\mathrm{i}\mathbf{k}(\mathbf{x}''-\mathbf{x}')}\,\mathrm{d}\mathbf{k}\right)\mathrm{d}\mathbf{x}'\,\mathrm{d}\mathbf{x}''. \tag{B.4}
$$

Using the definition of the Dirac function

$$
\frac{1}{(2\pi)^2}\int \mathrm{e}^{\mathrm{i}\mathbf{k}(\mathbf{x}''-\mathbf{x}')}\,\mathrm{d}\mathbf{k} = \delta(\mathbf{x}'-\mathbf{x}''), \tag{B.5}
$$

and the fact that $f^2 = G$, one simply gets

$$
\frac{1}{(2\pi)^2}\int \Re\left[\widehat{u'}(\mathbf{x},\mathbf{k},t)\widehat{\omega'}(\mathbf{x},-\mathbf{k},t)\right]\mathrm{d}\mathbf{k} = \overline{u'\omega'}(\mathbf{x},t). \tag{B.6}
$$

We may proceed along the same line for the average of the non-linear product of a large-scale field with a subfilter-scale field. Using the definition of the average $\overline{\mathbf{U}\omega'}(\mathbf{x},t)$ can be written as follows:

$$
\overline{\mathbf{U}\omega'}(\mathbf{x},t) = \int f^2(\epsilon^\star(\mathbf{x}-\mathbf{x}'))\mathbf{U}(\mathbf{x}',t)\omega'(\mathbf{x}',t)\,\mathrm{d}\mathbf{x}'. \tag{B.7}
$$

Using the Taylor expansion of U with respect to $\mathbf{x}$ at the first order, we obtain the first-order approximation of this term

$$
\overline{\mathbf{U}\omega'}(\mathbf{x},t) = (\mathbf{U}\overline{\omega'})(\mathbf{x}) + \int f^2(\epsilon^\star(\mathbf{x}-\mathbf{x}'))(\mathbf{x}-\mathbf{x}')\nabla\mathbf{U}(\mathbf{x}',t)\omega'(\mathbf{x}',t)\,\mathrm{d}\mathbf{x}' = (\mathbf{U}\overline{\omega'})(\mathbf{x}) + \mathrm{O}(\epsilon^\star). \tag{B.8}
$$

If we now apply the definition of the average for a product of two subfilter-scale fields (B.6) with the quantities "1" and ω', we finally obtain

$$\overline{\mathbf{U}\omega'}(\mathbf{x},t) = \mathbf{U}\frac{1}{(2\pi)^2} \int \Re\left[\widehat{\omega'}(\mathbf{x},\mathbf{k},t)\hat{1}(\mathbf{x},-\mathbf{k},t)\right] d\mathbf{k} + \mathrm{O}(\epsilon^\star) \tag{B.9}$$

$$= \mathbf{U}\frac{1}{(2\pi)^2} \int \Re\left[\widehat{\omega'}(\mathbf{x},\mathbf{k},t)\hat{f}(k)\right] d\mathbf{k} + \mathrm{O}(\epsilon^\star). \tag{B.10}$$

Appendix C. Numerical computation of the SFSA

The subfilter-scale field in physical space can be obtained from their discrete formula in the $(\mathbf{x},\mathbf{k})$ by an integration with respect to $\mathbf{k}$

$$\omega'(\mathbf{x},t) = \frac{1}{(2\pi)^2 f(0)} \int \widehat{\omega'}(\mathbf{x},\mathbf{k},t) \, d\mathbf{k} = \frac{1}{(2\pi)^2 f(0)} \int \sum_{\alpha=1}^{2N_p} \hat{\sigma}_\alpha(t) S_{\mathbf{x}}(\mathbf{x}-\mathbf{x}_\alpha(t))\delta(\mathbf{k}-\mathbf{k}_\alpha(t)) \, d\mathbf{k}$$

$$= \frac{1}{f(0)} \sum_{\alpha=1}^{2N_p} \hat{\sigma}_\alpha(t) S_{\mathbf{x}}(\mathbf{x}-\mathbf{x}_\alpha(t))$$

$$= \frac{1}{f(0)}\left\{ \sum_{\alpha_+=1}^{N_p} \hat{\sigma}_{\alpha_+}(t) S_{\mathbf{x}}(\mathbf{x}-\mathbf{x}_{\alpha_+}(t)) + \sum_{\alpha_-=1}^{N_p} \hat{\sigma}_{\alpha_1}(t) S_{\mathbf{x}}(\mathbf{x}-\mathbf{x}_{\alpha_-}(t)) \right\}, \tag{C.1}$$

where

$$\sum_{\alpha=1}^{2N_p} = \sum_{\alpha_+=1}^{N_p} + \sum_{\alpha_-=1}^{N_p}, \tag{C.2}$$

$\sum_{\alpha_+=1}^{N_p}$ means sum over half the particles with the wavenumber $\mathbf{k}_\alpha$ and $\sum_{\alpha_-=1}^{N_p}$ is the sum over particles with an opposite wavenumber $-\mathbf{k}_\alpha$. We choose the "positive" particles α_+ with $p_{\alpha_+} > 0$ and $\mathbf{k}_\alpha = (p_{\alpha_+}, q_{\alpha_+})$. Because $\mathbf{x}_{\alpha_+} = \mathbf{x}_{\alpha_-}$, $\omega'(\mathbf{x},t)$ can be written as

$$\omega'(\mathbf{x},t) = \frac{1}{f(0)} \sum_{\alpha_+=1}^{N_p} \left(\hat{\sigma}_{\alpha_+}(t) + \hat{\sigma}_{\alpha_-}(t) \right) S_{\mathbf{x}}(\mathbf{x}-\mathbf{x}_{\alpha_+}(t)). \tag{C.3}$$

Since $\omega'(\mathbf{x},t)$ is real, the following property holds:

$$\hat{\sigma}_{\alpha_+}(t) = \hat{\sigma}_{\alpha_-}^*(t) \tag{C.4}$$

and the formula used to rebuild the vorticity field in physical space is

$$\omega'(\mathbf{x},t) = \frac{2}{f(0)} \sum_{\alpha_+=1}^{N_p} \Re\left[\hat{\sigma}_{\alpha_+}(t)\right] S_{\mathbf{x}}(\mathbf{x}-\mathbf{x}_{\alpha_+}(t)), \tag{C.5}$$

where $\Re[\hat{\sigma}_{\alpha_+}(t)]$ is the real part of $\hat{\sigma}_{\alpha_+}(t)$. The same developments can be made for the two velocity component, using (B.2) and (B.3):

$$u'(\mathbf{x},t) = \frac{2}{f(0)} \sum_{\alpha_+=1}^{N_p} \frac{-q_{\alpha_+}}{p_{\alpha_+}^2 + q_{\alpha_+}^2} \Im\left[\hat{\sigma}_{\alpha_+}(t)\right] S_{\mathbf{x}}(\mathbf{x}-\mathbf{x}_{\alpha_+}(t)), \tag{C.6}$$

$$v'(\mathbf{x},t) = \frac{2}{f(0)} \sum_{\alpha_+=1}^{N_p} \frac{p_{\alpha_+}}{p_{\alpha_+}^2 + q_{\alpha_+}^2} \Im\left[\hat{\sigma}_{\alpha_+}(t)\right] S_{\mathbf{x}}(\mathbf{x}-\mathbf{x}_{\alpha_+}(t)), \tag{C.7}$$

where $\Im[\hat{\sigma}_{\alpha_+}(t)]$ is now the Imaginary part of $\hat{\sigma}_{\alpha_+}(t)$.

The previous expressions can be used to compute velocity correlations. Using the analytical definition of these terms with respect the the subfilter-scales field in $(\mathbf{x},\mathbf{k})$ space B.2,B.3, the derivation (B.6) apply to u' and v', and using the definition of the subfilter scale discretization (16), we get

$$\overline{u'v'}(\mathbf{x},t) = \frac{1}{(2\pi)^2} \int \Re\left[\widehat{u'}(\mathbf{x},\mathbf{k},t)\widehat{v'}(\mathbf{x},-\mathbf{k},t)\right]d\mathbf{k} = \frac{1}{(2\pi)^2} \int \Re\left[\left(\sum_{\alpha=1}^{2N_p} \frac{iq}{p^2+q^2}\hat{\sigma}_\alpha S_\mathbf{x}(\mathbf{x}-\mathbf{x}_\alpha)\delta(\mathbf{k}-\mathbf{k}_\alpha)\right)\right.$$

$$\left. \times \left(\sum_{\beta=1}^{2N_p} \frac{+ip}{p^2+q^2}\hat{\sigma}_\beta S_\mathbf{x}(\mathbf{x}-\mathbf{x}_\beta)\delta(-\mathbf{k}-\mathbf{k}_\beta)\right)\right]d\mathbf{k}. \tag{C.8}$$

If all the wave packets have different wavenumbers (at least on a domain equal to the "support" of S_x), Eq. (C.8) can be written as

$$\overline{u'v'}(\mathbf{x},t) = 2\sum_{\alpha_+=1}^{N_p} \Re\left[\frac{-q_{\alpha_+}p_{\alpha_+}}{(p_{\alpha_+}^2+q_{\alpha_+}^2)^2}\hat{\sigma}_{\alpha_+}\hat{\sigma}_{\alpha_-}S_\mathbf{x}^2(\mathbf{x}-\mathbf{x}_{\alpha_+})\right]. \tag{C.9}$$

Using the fact that $\hat{\sigma}_{\alpha_-}$ and $\hat{\sigma}_{\alpha_+}$ are complex conjugate, we finally get

$$\overline{u'v'}(\mathbf{x},t) = 2\sum_{\alpha_+=1}^{N_p} \frac{-q_{\alpha_+}p_{\alpha_+}}{(p_{\alpha_+}^2+q_{\alpha_+}^2)^2}|\hat{\sigma}_{\alpha_+}|^2 S_\mathbf{x}^2(\mathbf{x}-\mathbf{x}_{\alpha_+}),$$

$$\overline{u'^2}(\mathbf{x},t) = 2\sum_{\alpha_+=1}^{N_p} \frac{+q_{\alpha_+}^2}{(p_{\alpha_+}^2+q_{\alpha_+}^2)^2}|\hat{\sigma}_{\alpha_+}|^2 S_\mathbf{x}^2(\mathbf{x}-\mathbf{x}_{\alpha_+}), \tag{C.10}$$

$$\overline{v'^2}(\mathbf{x},t) = 2\sum_{\alpha_+=1}^{N_p} \frac{+p_{\alpha_+}^2}{(p_{\alpha_+}^2+q_{\alpha_+}^2)^2}|\hat{\sigma}_{\alpha_+}|^2 S_\mathbf{x}^2(\mathbf{x}-\mathbf{x}_{\alpha_+}).$$

The non-linear term involving the resolved-scale velocity field can also be written in terms of wave packet coordinates. Using Eq. (B.10) and the definition of discretization (16), one can write

$$\overline{\mathbf{U}\omega'}(\mathbf{x},t) \simeq \frac{\mathbf{U}}{(2\pi)^2} \int \Re\left[\widehat{\omega'}(\mathbf{x},\mathbf{k},t)\hat{1}(\mathbf{x},-\mathbf{k},t)\right]d\mathbf{k} \simeq \frac{\mathbf{U}}{(2\pi)^2} \int \Re\left[\widehat{\omega'}(\mathbf{x},\mathbf{k},t)f(-\mathbf{k})\right]d\mathbf{k}$$

$$\simeq \frac{\mathbf{U}}{(2\pi)^2} \int \Re\left[\sum_{\alpha=1}^{2N_p} \widehat{\sigma_\alpha}f^*(\mathbf{k})S_\mathbf{x}(\mathbf{x}-\mathbf{x}_\alpha)\delta(\mathbf{k}-\mathbf{k}_\alpha)\right]d\mathbf{k}$$

$$\simeq 2\mathbf{U}\sum_{\alpha_+=1}^{N_p} \Re\left[\widehat{\sigma_{\alpha_+}}f^*(\mathbf{k}_{\alpha_+})\right]S_\mathbf{x}(\mathbf{x}-\mathbf{x}_{\alpha_+}). \tag{C.11}$$

Appendix D. Choice of the filter

The choice of the interpolating function $S_x(\mathbf{x})$ (Eq. (17)) dictates the shape of the filter and therefore of the unknown function $f(x)$ in the definition of the Gabor transform. The proof proceeds via the quantity $\overline{\omega'^2}(\mathbf{x},t)$, by equating the formula of the filter discretized on a regular grid with a cell size $\Delta\mathbf{x}$ and the formula (C.5):

$$\overline{\omega'^2}(\mathbf{x},t) = \sum_i \omega'^2(\mathbf{x}_i)f^2(\mathbf{x}-\mathbf{x}_i)(\Delta\mathbf{x})^2, \tag{D.1}$$

$$= 2\sum_{\alpha_+=1}^{N_p} |\sigma_{\alpha_+}|^2 S_\mathbf{x}^2(\mathbf{x}-\mathbf{x}_{\alpha_+}). \tag{D.2}$$

For this equality to be valid at all grid point X_i, the following relation between f and S must hold:

$$f^2(\mathbf{x}) = C \times S_\mathbf{x}^2(\mathbf{x}). \tag{D.3}$$

Using now the normalization

$$S_\mathbf{x}(0) = 1, \tag{D.4}$$

$$\int f^2(\mathbf{x}')\,\mathrm{d}\mathbf{x}' = 1. \tag{D.5}$$

Eq. (D.3) becomes

$$f(\mathbf{x}) = f(0)S_\mathbf{x}(\mathbf{x}) \tag{D.6}$$

with

$$f(0) = \frac{1}{\sqrt{\int S_\mathbf{x}^2(\mathbf{x}')\,\mathrm{d}\mathbf{x}'}}. \tag{D.7}$$

References

[1] A. Leonard, in: T. Gatski (Ed.), Direct Numerical Simulations, in Turbulence and its Simulation, Springer, Berlin, 1995.
[2] J. Werne, D.C. Fritts, Stratified shear turbulence: evolution and statistics, Geophys. Res. Lett. 26 (1999) 439–442.
[3] R.D. Joslin, Discussion of DNS: past, present and future, in: First International Conference on Direct Numerical Simulation and Large Eddy Simulation (DNS/LES), Ruston, Louisiana, 1997.
[4] S. Grossmann, D. Lohse, A. Reech, Developped turbulence: from full simulations to full mode reductions, Phys. Rev. Lett. 77 (1996) 5369–5372.
[5] M. Meneguzzi, H. Politano, A. Pouquet, M. Zolver, A sparse-mode spectral method for the simulation of turbulent flows, J. Comput. Phys. 123 (1996) 32–44.
[6] K. Schneider, N.K.-R. Kevlahan, M. Farge, Comparison of an adaptative wavelet method and nonlinearly filtered pseudospectral methods for two-dimensional turbulence, Theor. Comput. Fluid Dyn. 9 (1997) 191–206.
[7] M.J. Berger, J. Oliger, Adaptative mesh refinement for hyperbolic partial differential equations, J. Comput. Phys. 53 (1984) 484.
[8] M.J. Berger, P. Collela, Local adaptative mesh refinement for shock hydrodynamics, J. Comput. Phys. 82 (1989) 64.
[9] M. Oberlack, Unified theory for symmetries in plane parallel turbulent shear flows, J. Fluids Mech. 427 (2001).
[10] J.-P. Laval, B. Dubrulle, S. Nazarenko, Dynamical modeling of sub-grid scales in 2D turbulence, Physica D 142 (2000) 231–253.
[11] J.-P. Laval, B. Dubrulle, S. Nazarenko, Nonlocality of interaction of scales in the dynamics of 2D incompressible fluids, Phys. Rev. Lett. 83 (1999) 4061–4064.
[12] J.-P. Laval, B. Dubrulle, J.C. McWilliams, Langevin models of turbulence: renormalization group, distant interaction algorithms or rapid distortion theory?, Phys. Fluids 15 (5) (2003) 1327–1339.
[13] S. Nazarenko, N.K.-R. Kevlahan, B. Dubrulle, Nonlinear RDT theory of near-wall turbulence, Physica D 139 (2000) 158–176.
[14] S. Nazarenko, N.K.-R. Kevlahan, B. Dubrulle, HWKB theory for rapid distortion of homogeneous turbulence, J. Fluid Mech. 390 (1999) 325–348.
[15] B. Dubrulle, J.-P. Laval, S.V. Nazarenko, N.K.-R. Kevlahan, A dynamic subfilter-scale model for plane parallel flows, Phys. Fluids 13 (2001) 2045–2064.

[16] B. Dubrulle, P. Laval, J.-P. Sullivan, J. Werne, A new dynamical subgrid model for the planetary surface layer. I. The model, J. Atmos. Sci. 59 (2002) 857–872.

[17] B. Dubrulle, J.-P. Laval, P. Sullivan, A new dynamical subgrid model for the planetary surface layer. II. Analytical computations of fluxes, mean profiles and variances, J. Atmos. Sci. 59 (2002) 873–887.

[18] S. Nazarenko, J.-P. Laval, Non-local 2D turbulence and Batchelor's regime for passive scalars, J. Fluid Mech. 408 (2000) 301–321.

[19] J.-P. Laval, B. Dubrulle, S. Nazarenko, Non-locality and intermittency in three-dimensional turbulence, Phys. Fluids 13 (2001) 1995–2012.

[20] M.E. Brachet, M. Meneguzzi, H. Politano, P.L. Sulem, The dynamics of freely decaying two-dimensional turbulence, J. Fluid Mech. 194 (1988) 333–349.

[21] M. Farge, N.K.-R. Kevlahan, V. Perrier, E. Goirand, Wavelets and turbulence, Proc. IEEE 84 (1996) 639–669.

[22] M. Farge, K. Schneider, N.K.-R. Kevlahan, Non-gaussianity and coherent vortex simulation for two-dimensional turbulence using an adaptadive orthogonal wavelet basis, Phys. Fluids 11 (1999) 2187–2201.

[23] S. Nazarenko, N. Zabusky, T. Scheidegger, Nonlinear sound–vortex interactions in an inviscid isentropic fluid: a two fluid model, Phys. Fluids 7 (1995) 2407.

[24] R. Sadourny, C. Basdevant, Parametrization of subgrid scale barotropic eddies in quasi-geotrophic models: anticipated potential vorticity method, J. Atmos. Sci. 42 (1985) 1353–1363.

[25] A. Babiano, C. Basdevant, B. Legras, R. Sadourny, Vorticity and passive scalar dynamics in two-dimensional turbulence, J. Fluid Mech. 183 (1987) 379–397.

[26] A. Babiano, B. Dubrulle, P. Frick, Scaling properties of numerical two-dimensional turbulence, Phys. Rev. E 52 (1995) 3719–3729.

[27] P. Bartello, T. Warn, Self-similarity of decaying two-dimensional turbulence, J. Fluid Mech. 326 (1996) 357–372.

[28] A. Mariotti, B. Legras, D.G. Dritschel, Vortex stripping and erosion of coherent structures in two-dimensional flows, Phys. Fluids 6 (1994) 3954–3962.